

Article

The Cobalt(II) Oxidotellurate(IV) Hydroxides $\text{Co}_2(\text{TeO}_3)(\text{OH})_2$ and $\text{Co}_{15}(\text{TeO}_3)_{14}(\text{OH})_2$

Felix Eder ¹, Matthias Weil ^{1,*}, Prativa Pramanik ² and Roland Mathieu ²

¹ Institute for Chemical Technologies and Analytics, Division of Structural Chemistry, TU Wien, Getreidemarkt 9/164-5-01, 1060 Vienna, Austria

² Department of Materials Science and Engineering, Uppsala University, Box 35, 751 03 Uppsala, Sweden

* Correspondence: matthias.weil@tuwien.ac.at

Abstract: Previously unknown $\text{Co}_2(\text{TeO}_3)(\text{OH})_2$ and $\text{Co}_{15}(\text{TeO}_3)_{14}(\text{OH})_2$ were obtained under mild hydrothermal reaction conditions (210 °C, autogenous pressure) from alkaline solutions. Their crystal structures were determined from single-crystal X-ray diffraction data. $\text{Co}_2(\text{TeO}_3)(\text{OH})_2$ ($Z = 2$, $P\bar{1}$, $a = 5.8898(5)$, $b = 5.9508(5)$, $c = 6.8168(5)$ Å, $\alpha = 101.539(2)$, $\beta = 100.036(2)$, $\gamma = 104.347(2)^\circ$, 2120 independent reflections, 79 parameters, $R[F^2 > 2\sigma(F^2)] = 0.017$) crystallizes in a unique structure comprised of undulating ${}^2_\infty[\text{Co}_2(\text{OH})_{6/3}\text{O}_{3/3}\text{O}_{2/2}\text{O}_{1/1}]^{4-}$ layers. Adjacent layers are linked by Te^{IV} atoms along the [001] stacking direction. $\text{Co}_2(\text{TeO}_3)(\text{OH})_2$ is stable up to 450 °C and decomposes under the release of water into $\text{Co}_6\text{Te}_5\text{O}_{16}$ and CoO. Magnetic measurements of $\text{Co}_2(\text{TeO}_3)(\text{OH})_2$ showed antiferromagnetic ordering at ≈ 70 K. The crystal structure of $\text{Co}_{15}(\text{TeO}_3)_{14}(\text{OH})_2$ ($Z = 3$, $R\bar{3}$, $a = 11.6453(2)$, $c = 27.3540(5)$ Å, 3476 independent reflections, 112 parameters, $R[F^2 > 2\sigma(F^2)] = 0.026$) is isotypic with $\text{Co}_{15}(\text{TeO}_3)_{14}\text{F}_2$. A quantitative structural comparison revealed that the main structural difference between the two phases is connected with the replacement of F by OH, whereas the remaining part of the three-periodic network defined by $[\text{CoO}_6]$, $[\text{CoO}_5(\text{OH})]$, $[\text{CoO}_5]$ and $[\text{TeO}_3]$ polyhedra is nearly unaffected. Consequently, the magnetic properties of the two phases are similar, namely being antiferromagnetic at low temperatures.



Citation: Eder, F.; Weil, M.; Pramanik, P.; Mathieu, R. The Cobalt(II) Oxidotellurate(IV) Hydroxides $\text{Co}_2(\text{TeO}_3)(\text{OH})_2$ and $\text{Co}_{15}(\text{TeO}_3)_{14}(\text{OH})_2$. *Crystals* **2023**, *13*, 176. <https://doi.org/10.3390/cryst13020176>

Academic Editors: Lilianna Chęcinska and Magdalena Matecka

Received: 22 December 2022

Revised: 11 January 2023

Accepted: 12 January 2023

Published: 19 January 2023



Copyright: © 2023 by the authors. Licensee MDPI, Basel, Switzerland. This article is an open access article distributed under the terms and conditions of the Creative Commons Attribution (CC BY) license (<https://creativecommons.org/licenses/by/4.0/>).

Keywords: cobalt; tellurium; structure determination; structural similarity; magnetic properties; thermal behavior

1. Introduction

Cobalt compounds in the ternary Co/Te/O system are known to exist solely with an oxidation state of +II for Co, whereas the oxidation state of Te can be +IV or +VI. Next to the structural variety of corresponding cobalt(II) oxidotellurates resulting from the two possible oxidation states of Te and the condensation grade of the oxidotellurate anions, some of the phases in this system are of interest due to their interesting magnetic and electronic behaviors. This includes $\text{CoTe}^{\text{IV}}\text{O}_3$ [1,2], $\text{CoTe}^{\text{VI}}\text{O}_4$ [3], $\text{Co}_3\text{Te}^{\text{VI}}\text{O}_6$ [4–8] and $\text{Co}_5\text{Te}^{\text{VI}}\text{O}_8$ [9]. Most of these phases have been prepared by conventional solid-state reactions at varying pressure conditions [1–4,7–9], or by the application of chemical vapor transport reactions [5,6,10]. Other phases in the Co/Te/O system, for which crystal structure determinations have been carried out so far, include $\text{Co}_6\text{Te}^{\text{IV}}\text{O}_{16}$ [11], $\text{CoTe}^{\text{IV}}\text{O}_{13}$ [12] and $\text{Co}_2\text{Te}^{\text{IV}}\text{O}_8$ [13]. The latter two phases were prepared by hydrothermal synthesis. Under the conditions typically applied for this method, an incorporation of water or OH groups into the resulting solids is not uncommon, which, in the case of cobalt oxidotellurates, yielded non-centrosymmetric $\text{Co}_3(\text{Te}^{\text{IV}}\text{O}_3)_2(\text{OH})_2$ [14]. Subsequent re-investigations of this phase likewise revealed interesting magnetic and electric properties [15], as well as a possible incorporation of foreign components into the channels of the crystal structure, where parts of the OH groups can be replaced by other anions and/or water molecules [16]. During the latter study and during related hydrothermal formation studies for phases with zemannite-type structures [17], we

obtained two new cobalt(II) oxidotellurates(IV) with additional OH groups in the form of side products, viz. $\text{Co}_2(\text{TeO}_3)(\text{OH})_2$ and $\text{Co}_{15}(\text{TeO}_3)_{14}(\text{OH})_2$.

We report here on our efforts to increase the yield of $\text{Co}_2(\text{TeO}_3)(\text{OH})_2$ and $\text{Co}_{15}(\text{TeO}_3)_{14}(\text{OH})_2$, together with the results of their crystal structure analyses and physical property measurements.

2. Materials and Methods

2.1. Synthesis

All employed chemicals were of *pro analysi* quality and were purchased from Merck (Darmstadt, Germany). $\text{Co}_2(\text{TeO}_3)(\text{OH})_2$ and $\text{Co}_{15}(\text{TeO}_3)_{14}(\text{OH})_2$ were originally obtained as minor by-products during hydrothermal phase formation studies for the intended synthesis of $\text{Co}_3(\text{TeO}_3)_2(\text{OH})_2$ [16] or $\text{Na}_2[\text{Co}_2(\text{TeO}_3)_3]\cdot 3\text{H}_2\text{O}$ [17]. In representative experiments targeted for 0.5 g of the intended phase, CoCO_3 , TeO_2 and KOH (molar ratio 3:2:4) and CoO (prepared by thermal decomposition of CoCO_3), TeO_2 and Na_2CO_3 (molar ratio 2:3:10), respectively, were mixed and placed in Teflon containers with an inner volume of ≈ 4 mL. The containers were subsequently filled to two-thirds of their volume with water, sealed, placed in steel autoclaves and were heated under autogenous pressure for one week at 210 °C. The obtained solid products were filtered off with a glass frit, washed with water and ethanol and then dried in air. The obtained crystals could be distinguished due to their different colors and forms. $\text{Co}_2(\text{TeO}_3)(\text{OH})_2$ crystallizes in the form of pink needles up to 0.5 mm in lengths, $\text{Co}_{15}(\text{TeO}_3)_{14}(\text{OH})_2$ in form of dark blue-to-violet isometric crystals up to 0.2 mm in length (Figure 1), and both $\text{Na}_2[\text{Co}_2(\text{TeO}_3)_3]\cdot 3\text{H}_2\text{O}$ and $\text{Co}_3(\text{TeO}_3)_2(\text{OH})_2$ in form of violet thin hexagonal prisms.

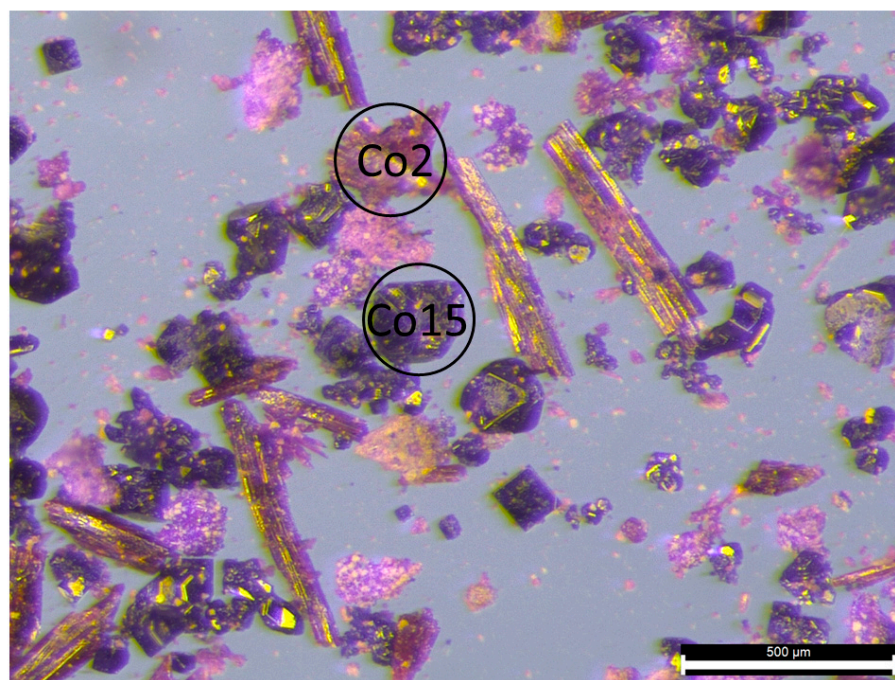


Figure 1. Typical crystal forms of hydrothermally grown crystals of $\text{Co}_2(\text{TeO}_3)(\text{OH})_2$ (designated as Co2 in the inset) and $\text{Co}_{15}(\text{TeO}_3)_{14}(\text{OH})_2$ (Co15).

Powder X-ray diffraction (PXRD) measurements of the bulk products revealed $\text{Co}_{15}(\text{TeO}_3)_{14}(\text{OH})_2$, $\text{Co}_2(\text{TeO}_3)(\text{OH})_2$ and $\text{Co}_3(\text{TeO}_3)_2(\text{OH})_2$ in approximate weight percentages of 58%, 27% and 15%, respectively, for the batch with CoCO_3 , TeO_2 and KOH . For the batch starting with CoO , TeO_2 and Na_2CO_3 , the products were $\text{Na}_2[\text{Co}_2(\text{TeO}_3)_3]\cdot 3\text{H}_2\text{O}$, $\text{Co}_{15}(\text{TeO}_3)_{14}(\text{OH})_2$ and $\text{Co}_3(\text{TeO}_3)_2(\text{OH})_2$ in approximate weight percentages of 60%, 25% and 15%, respectively.

Increasing the amount of KOH to a $\text{CoCO}_3:\text{TeO}_2:\text{KOH}$ ratio of 3:2:9 led to a brownish polycrystalline product that was leached with diluted sulfuric acid (0.1 M) for ten minutes at room temperature. After the remaining solid was filtered off and washed with water and ethanol, a change to a dark pink color was observed. This product corresponds to single-phase $\text{Co}_2(\text{TeO}_3)(\text{OH})_2$.

For subsequent physical measurements, single-phase material of polycrystalline $\text{Co}_2(\text{TeO}_3)(\text{OH})_2$ was used, whereas for $\text{Co}_{15}(\text{TeO}_3)_{14}(\text{OH})_2$ single crystals were hand-picked under an optical microscope.

2.2. X-ray Diffraction Measurements and Crystal-Structure Analysis

PXRD measurements were performed on a PANalytical X'Pert II Pro-type PW 3040/60 diffractometer using $\text{Cu-K}_{\alpha 1,2}$ -radiation and an X'Celerator detector (Malvern Panalytical, Malvern, United Kingdom). For phase analysis of the reaction products, the Highscore+ software suite [18] (version 5.1) was employed.

Single-crystal X-ray diffraction measurements were performed on a Bruker Kappa APEX II single-crystal diffractometer using graphite-monochromatized Mo-K_{α} radiation equipped with a CCD detector (Bruker AXS, Madison, WI, USA). Instrument software (Apex-4, Saint [19]) was used for optimized measurement strategies (>99% completeness at θ_{max}) and for data reduction; correction for absorption effects was performed with SAD-ABS [20]. The crystal structures were solved with SHELXT [21], refined with SHELXL [22] and graphically represented with ATOMS [23]. In the case of $\text{Co}_2(\text{TeO}_3)(\text{OH})_2$, hydrogen atoms, which are part of an OH group, could clearly be located from a difference-Fourier map. Their positions were freely refined with $U_{\text{iso}}(\text{H}) = 1.5U_{\text{eq}}$ of the parent O atom. In the case of $\text{Co}_{15}(\text{TeO}_3)_{14}(\text{OH})_2$, the hydrogen atom of the OH group could not be located and thus is not part of the structure model. For the latter structure, atom labels and coordinates were assigned in accordance with the previously reported isotypic crystal structure of $\text{Mn}_{15}(\text{TeO}_3)_{14}(\text{OH})_2$ [24].

Crystal structures and refinement data are listed in Table 1. Further details of the crystal structure investigations may be obtained from the joint CCDC/FIZ Karlsruhe online deposition service: <https://www.ccdc.cam.ac.uk/structures/> by quoting the deposition numbers specified at the end of Table 1.

Bond valence sums (BVS) [25] were calculated using the bond valence parameters provided by Brese & O'Keeffe [26]. For the $\text{Te}^{\text{IV}}\text{-O}$ pair, the revised bond valence parameters by Mills & Christy [27] were additionally used, then they were put under consideration of all oxygen atoms within a distance of 3.5 Å.

Isotypic structures were quantitatively compared using the *compstru* program [28] available at the Bilbao crystallographic server [29].

2.3. Magnetic Measurements

The magnetic properties of the two materials were investigated as a function of temperature and magnetic field using a superconducting quantum interference device (SQUID) magnetometer from Quantum Design Inc (San Diego, CA, USA).

2.4. IR Spectroscopy

IR measurements were carried out in an ATR set-up on a Perkin Elmer Spectrum Two FT-IR spectrometer (with a diamond UATR unit; Perkin Elmer, Waltham, MA, USA). After the determination of the background (air), transmission was recorded in a range of 4000–400 cm^{-1} . Samples were ground to fine powder prior to the investigation. The spectra were obtained as an average of four consecutive individual measurements.

2.5. Thermal Analysis

Thermogravimetry (TG) and differential scanning calorimetry (DSC) measurements were carried out in the temperature range 30–580 °C under flowing argon atmosphere (20 mL min^{-1}) conditions on a Netzsch TG 209 F3 Tarsus (heating rate 10 °C· min^{-1}) and

a Netzsch DSC 200 F3 Maia instrument (heating/cooling rate $10\text{ }^{\circ}\text{C}\cdot\text{min}^{-1}$), respectively (Netzsch, Selb, Germany). For the TG measurements, an alumina crucible with an inner volume of $85\text{ }\mu\text{L}$ and with a pierced alumina lid was used as sample container. A correction measurement of the empty crucible was conducted and afterwards subtracted from the measurement data. For the DSC measurements, the samples were placed into aluminum crucibles (inner volume of $25\text{ }\mu\text{L}$) that were cold-welded with a pierced aluminum lid.

Table 1. Data collection and refinement details.

	$\text{Co}_2(\text{TeO}_3)(\text{OH})_2$	$\text{Co}_{15}(\text{TeO}_3)_{14}(\text{OH})_2$
M_r	654.95	3376.37
Space group, No	$P\bar{1}$, 2	$R\bar{3}$, 148
Z	1	3
Temperature/ $^{\circ}\text{C}$	−173	23
Crystal form, color	lath, pink	block, dark blue
Crystal size/ mm^3	$0.14 \times 0.04 \times 0.03$	$0.11 \times 0.09 \times 0.06$
$a/\text{\AA}$	5.8898(5)	11.6453(2)
$b/\text{\AA}$	5.9508(5)	11.6453(2)
$c/\text{\AA}$	6.8168(5)	27.3540(5)
$\alpha/^{\circ}$	101.539(2)	90
$\beta/^{\circ}$	100.036(2)	90
$\gamma/^{\circ}$	104.347(2)	120
$V/\text{\AA}^3$	220.40(3)	3212.57(12)
X-ray density/ $\text{g}\cdot\text{cm}^{-3}$	4.935	5.236
Radiation type	Mo $K\alpha$	Mo $K\alpha$
μ/mm^{-1}	13.92	15.11
T_{\min}, T_{\max}	0.350, 0.568	0.294, 0.438
Diffractometer	Bruker AXS APEX-II	Bruker AXS APEX-II
Absorption correction	SADABS [20]	SADABS [20]
No. of measured, independent and observed [$I > 2\sigma(I)$] reflections	6273 2120 2068	17537 3476 2875
R_{int}	0.020	0.051
$(\sin \theta/\lambda)_{\text{max}}/\text{\AA}^{-1}$	0.833	0.834
No. of reflections	2120	3476
No. of parameters	79	112
H-atom treatment	H-atom coordinates refined	H-atom parameters not defined
$R[F^2 > 2\sigma(F^2)], wR(F^2), S$	0.017, 0.044, 1.19	0.026, 0.051, 1.02
$\Delta\rho_{\text{max}}, \Delta\rho_{\text{min}}$ ($\text{e}\text{\AA}^{-3}$)	1.13, −1.70	1.40, −1.38
CSD-code	2226560	2226561

3. Results and Discussion

3.1. Synthesis

PXRD of the product, formed from the more highly concentrated KOH solution, revealed single-phase $\text{Co}_2(\text{TeO}_3)(\text{OH})_2$ (see Supplementary Figure S1). In comparison with the other formed phases containing an additional OH group, i.e., $\text{Co}_{15}(\text{TeO}_3)_{14}(\text{OH})_2$ and $\text{Co}_3(\text{TeO}_3)_2(\text{OH})_2$, the amount of OH in $\text{Co}_2(\text{TeO}_3)(\text{OH})_2$ is the highest. Consequently, an increase in the OH^- concentration of the solution favors the formation of this product. On the other hand, $\text{Na}_2[\text{Co}_2(\text{TeO}_3)_3]\cdot 3\text{H}_2\text{O}$ without OH groups in the structure solely forms in Na_2CO_3 -containing solutions. Needless to say that this compound requires Na^+ cations to be formed, but the lower alkalinity of the soda solution compared to the caustic potash solution appears to govern that $\text{Co}_2(\text{TeO}_3)(\text{OH})_2$ is not formed from Na_2CO_3 solutions.

3.2. Crystal Structures

All atoms in the asymmetric unit of $\text{Co}_2(\text{TeO}_3)(\text{OH})_2$ (two Co, one Te, five O, two H) are situated on a general $2i$ position of space group $P\bar{1}$. Each of the two Co^{II} atoms is surrounded by six O atoms in form of a distorted octahedron, whereby Co1 shows a

coordination with four OH groups (associated with O1 and O2) and two O ligands, and Co2 does so with two OH groups and four O ligands. The $[\text{Co1}(\text{OH})_4\text{O}_2]$ octahedron shows a more disparate bond lengths distribution (with one considerably longer bond of 2.3422(17) Å to an O ligand) than the $[\text{Co2}(\text{OH})_2\text{O}_4]$ octahedron. Nevertheless, the average Co—O distances of 2.124 Å for Co1 and of 2.110 Å for Co2 are similar and match with the overall mean value of 2.108(62) Å, calculated for 243 $[\text{CoO}_6]$ polyhedra [30]. The $[\text{Co1}(\text{OH})_4\text{O}_2]$ octahedra are fused together by edge-sharing their OH groups, leading to the formation of $^1_\alpha[\text{Co1}(\text{OH})_{4/2}\text{O}_{2/1}]$ chains propagating parallel to [010]. Two $[\text{Co2}(\text{OH})_2\text{O}_4]$ octahedra are linked into centrosymmetric dimers through a common edge (O4—O4). These $[\text{Co2}(\text{OH})_{2/1}\text{O}_{2/2}\text{O}_{2/1}]_2$ dimers in turn link neighboring $^1_\alpha[\text{Co1}(\text{OH})_{4/2}\text{O}_{2/1}]$ chains through a common O1H—O2H edge and through corner-sharing the O4 and O5 atoms, thereby forming undulating layers $^2_\alpha[\text{Co}_2(\text{OH})_{6/3}\text{O}_{3/3}\text{O}_{2/2}\text{O}_{1/1}]^{4-}$ extending parallel to (001). In these layers, both OH groups are bonded to three Co^{II} atoms (Figure 2).

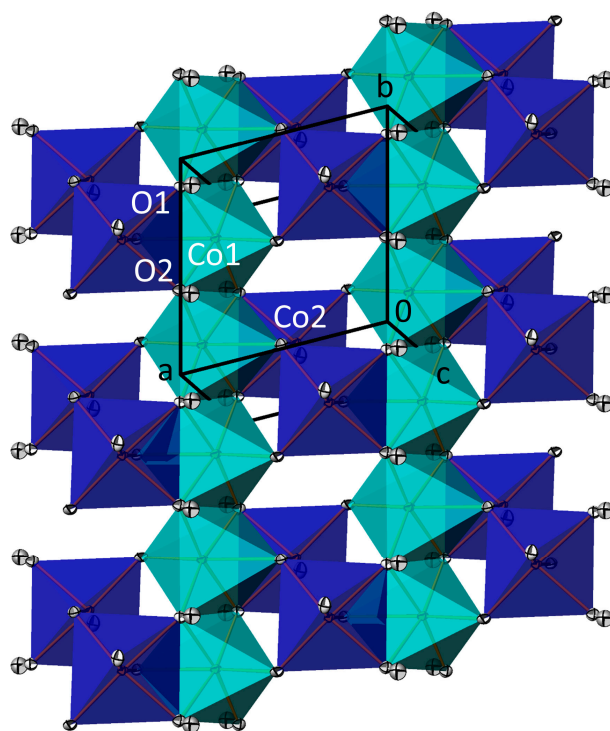


Figure 2. A perpendicular view of the $^2_\alpha[\text{Co}_2(\text{OH})_{6/3}\text{O}_{3/3}\text{O}_{2/2}\text{O}_{1/1}]^{4-}$ layer in the crystal structure of $\text{Co}_2(\text{TeO}_3)(\text{OH})_2$. The $[\text{Co1O}_6]$ octahedron is given in turquoise, the $[\text{Co2O}_6]$ octahedron in dark blue. Atoms are displayed with anisotropic displacement ellipsoids at a 90% probability level.

The $^2_\alpha[\text{Co}_2(\text{OH})_{6/3}\text{O}_{3/3}\text{O}_{2/2}\text{O}_{1/1}]^{4-}$ layers stack along [001] and are linked through the Te1^{IV} atoms that flank the layers on both sides. The Te1 atom is bonded to three O atoms in the shape of a trigonal pyramid, the most common coordination polyhedron for a $[\text{TeO}_3]$ unit [31]. In the crystal structure (Figure 3), the $[\text{TeO}_3]$ units are isolated from each other, having a connectivity of Q^{3000} in the notations of Christy et al. [31].

Additional stabilization of the structural arrangement is provided by a medium-strong hydrogen bond between one of the OH groups in one layer and an O atom in an adjacent layer ($\text{HO2}\cdots\text{O3} = 2.7296(19)$ Å). Interestingly, the second OH group (O1) has no potential acceptor O atom in a distance < 3.5 Å and apparently does not participate in hydrogen bonding interactions. The two kinds of hydrogen bonding interactions are reflected in the BVS values. Atom O3 shows considerable underbonding (Table 2) that is compensated for by its role as an acceptor atom of a medium-strong hydrogen bond. The BVS values of the other potential acceptor atoms O4 and O5 are close to the expected valence of -2 , and thus involvement in a noticeable hydrogen bonding interaction is not observed. The BVS

values of the Te and the two Co atoms deviate only slightly from the expected values of +4 and +2, respectively.

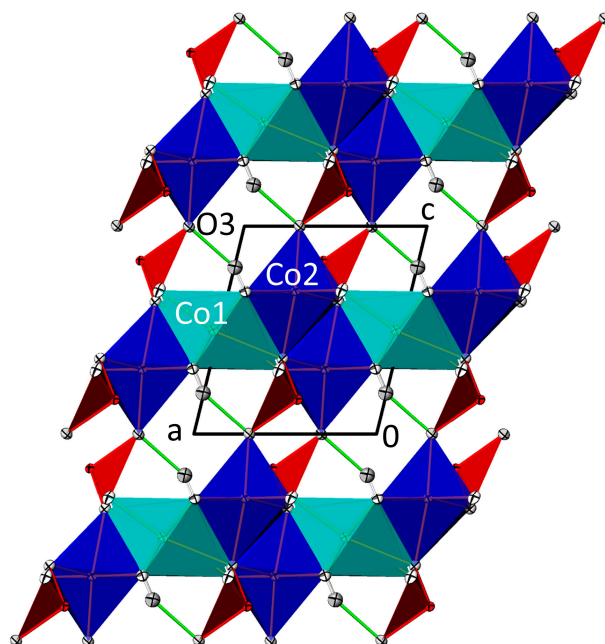


Figure 3. The crystal structure of $\text{Co}_2(\text{TeO}_3)(\text{OH})_2$ in a projection along $[010]$. $[\text{TeO}_3]$ polyhedra are red; $\text{O}-\text{H}\cdots\text{O}$ hydrogen bonding interactions are indicated by green lines. Other color codes and displacement ellipsoids are as in Figure 2.

The crystal structure of $\text{Co}_2(\text{TeO}_3)(\text{OH})_2$ shows a strong topological relationship to the selenium(IV) analog $\text{Co}_2(\text{SeO}_3)(\text{OH})_2$ [32]. Both crystal structures comprise the same set-up of chains and dimers condensed into layers, which are interlinked by the chalcogen(IV) atoms and consolidated by a hydrogen bond of the type $\text{O}-\text{H}\cdots\text{O}$. However, the crystal systems of the two structures are different, viz. triclinic ($P\bar{1}$, $Z = 2$) for the tellurium and monoclinic ($P2_1/n$, $Z = 4$) for the selenium compound.

The crystal structure of $\text{Co}_{15}(\text{TeO}_3)_{14}(\text{OH})_2$ (Figure 4) is isotypic with those of $\text{Mn}_{15}(\text{TeO}_3)_{14}(\text{OH})_2$ [23] and $\text{Co}_{15}(\text{TeO}_3)_{14}\text{F}_2$ [33]. Since the latter two crystal structures have been discussed in detail, we describe here only the main features. The asymmetric unit of $\text{Co}_{15}(\text{TeO}_3)_{14}(\text{OH})_2$ comprises three Co, three Te, and eight O atoms (the H atom was not determined). Atoms Te3 and O8 are located at sites with symmetry 3. (Wyck-off position $6c$), Mn2 at a site with symmetry $\bar{1}$ ($9e$), and all other atoms at a general site ($18f$) of space group $R\bar{3}$. Each of the three Te atoms is coordinated by three oxygen atoms, with distances between 1.86 and 1.89 Å, in the form of a trigonal pyramid. Like in $\text{Co}_2(\text{TeO}_3)(\text{OH})_2$, the correspondent $[\text{TeO}_3]$ units are isolated from each other in the crystal structure of $\text{Co}_{15}(\text{TeO}_3)_{14}(\text{OH})_2$, thus having a connectivity of Q^{3000} [31].

Co1 and Co3 exhibit a coordination number of 6, with a distorted octahedral arrangement of the oxygen ligands. The average Co–O distances of 2.106 Å and 2.102 Å, respectively, perfectly agree with the overall mean of 2.108(62) Å [30]. Co2 exhibits a $[4 + 1]$ coordination with five O atoms, with one considerably longer Co–O distance (2.332(2) Å) than the other four (1.989(2)–2.058(2) Å). Again, the average Co–O distance of 2.085 Å matches with the reference value of 2.066(177) Å, calculated for 16 $[\text{CoO}_5]$ polyhedra [30]. In $\text{Co}_{15}(\text{TeO}_3)_{14}(\text{OH})_2$, the shape of the resulting $[\text{Co}_2\text{O}_5]$ coordination polyhedron is closer to a (distorted) square pyramid than to a trigonal bipyramid, as expressed by the τ_5 descriptor [34] of 0.391 ($\tau_5 = 0$ for an ideal square pyramid and $\tau_5 = 1$ for an ideal trigonal bipyramid). The $[\text{CoO}_6]$, $[\text{CoO}_5\text{OH}]$ and $[\text{CoO}_5]$ polyhedra share corners and edges to assemble into a framework structure, with the Te^{IV} atoms and their associated non-bonding electron lone pairs occupying some of the remaining space (Figure 4).

The hydroxide group present in $\text{Co}_{15}(\text{TeO}_3)_{14}(\text{OH})_2$ is associated with the O8 atom (BVS 1.17 v.u.) and shows the shortest Co–O distance of the $[\text{Co}_3\text{O}_5\text{OH}]$ octahedron. All in all, O8 binds to three symmetry-related Co3 atoms. This situation is comparable to the O1 and O2 atoms in $\text{Co}_2(\text{TeO}_3)(\text{OH})_2$, but the mean (H)O–Co distances are considerably shorter in $\text{Co}_{15}(\text{TeO}_3)_{14}(\text{OH})_2$ (2.042 Å) than in $\text{Co}_2(\text{TeO}_3)(\text{OH})_2$ (2.105 and 2.078 Å).

The BVS values of the Co, Te, and the other O atoms are inconspicuous, with individual values slightly deviating from the expected valence of 2, 4 and –2, respectively (Table 2).

Table 2. Selected bond lengths/Å, angles/°, details of hydrogen bonding interactions as well as bond valence sums (BVS)/v.u. (values using the revised parameters for $\text{Te}^{\text{IV}}\text{–O}$ bonds [27] in parentheses).

$\text{Co}_2(\text{TeO}_3)(\text{OH})_2$				
Co1—O2	2.0320(13)		Co2—O5	2.0690(13)
Co1—O1	2.0569(13)		Co2—O3 ^v	2.0737(13)
Co1—O1 ⁱ	2.0912(13)		Co2—O2	2.0759(13)
Co1—O5 ⁱⁱ	2.1048(13)		Co2—O4 ^{vi}	2.1226(13)
Co1—O2 ⁱⁱⁱ	2.1239(13)		Co2—O4 ⁱⁱ	2.1449(13)
Co1—O4 ^{iv}	2.3433(13)		Co2—O1 ^{vi}	2.1722(13)
Te1—O3	1.8715(13)		O3—Te1—O5	98.32(6)
Te1—O5	1.8852(12)		O3—Te1—O4	94.73(6)
Te1—O4	1.8973(12)		O5—Te1—O4	98.82(5)
D—H...A	D—H	H...A	D...A	D—H...A
O2—				
H2...O3 ^{iv}	0.90(3)	1.87(3)	2.7296(19)	160(3)
BVS: Co1 1.93, Co2 1.95, Te1 3.86 (3.93), O1 1.00 (without H), O2 1.06 (without H), O3 1.61, O4 1.95, O5 1.90				
Symmetry codes: (i) $-x + 2, -y + 2, -z + 1$; (ii) $-x + 1, -y + 1, -z + 1$; (iii) $-x + 2, -y + 1, -z + 1$; (iv) $x + 1, y, z$; (v) $-x + 1, -y + 1, -z + 2$; (vi) $x, y - 1, z$.				
$\text{Co}_{15}(\text{TeO}_3)_{14}(\text{OH})_2$				
Co1—O5 ⁱ	2.018(2)		Te1—O1 ^{iv}	1.886(2)
Co1—O5 ⁱⁱ	2.018(2)		Te1—O1 ^v	1.886(2)
Co1—O4 ⁱⁱⁱ	2.141(2)		Te1—O1	1.886(2)
Co1—O4 ^{iv}	2.141(2)		Te2—O3	1.868(2)
Co1—O1 ⁱⁱ	2.159(2)		Te2—O2 ^v	1.877(2)
Co1—O1 ⁱ	2.159(2)		Te2—O5	1.896(2)
Co2—O3	1.989(2)		Te3—O6	1.855(2)
Co2—O7 ⁱ	2.019(2)		Te3—O4	1.866(2)
Co2—O1	2.024(2)		Te3—O7 ^v	1.889(2)
Co2—O5 ^{iv}	2.058(2)		O1 ^{iv} —Te1—O1 ^v	98.58(9)
Co2—O2	2.331(2)		O1—Te1—O1 ^{iv}	98.58(9)
Co3—O8	2.0419(6)		O1—Te1—O1 ^v	98.58(9)
Co3—O2 ⁱ	2.046(2)		O3—Te2—O2 ^v	91.85(10)
Co3—O2	2.083(2)		O3—Te2—O5	94.86(10)
Co3—O3	2.102(2)		O2 ^v —Te2—O5	87.18(10)
Co3—O6	2.141(2)		O6—Te3—O4	99.11(11)
Co3—O7	2.202(2)		O6—Te3—O7 ^v	98.75(10)
			O4—Te3—O7 ^v	98.95(10)
BVS: Co1 1.99, Co2 1.82, Co3 2.00, Te1 3.85 (3.89), Te2 3.89 (4.01), Te3 4.01 (3.81), O1 1.89, O2 2.13, O3 2.03, O4 1.85, O5 2.05, O6 1.85, O7 1.86, O8 1.17.				
Symmetry codes: (i) $-x + 2/3, -y + 1/3, -z + 1/3$; (ii) $x + 1/3, y - 1/3, z - 1/3$; (iii) $x - y + 1, x, -z$; (iv) $-x + y, -x, z$; (v) $-y, x - y, z$.				

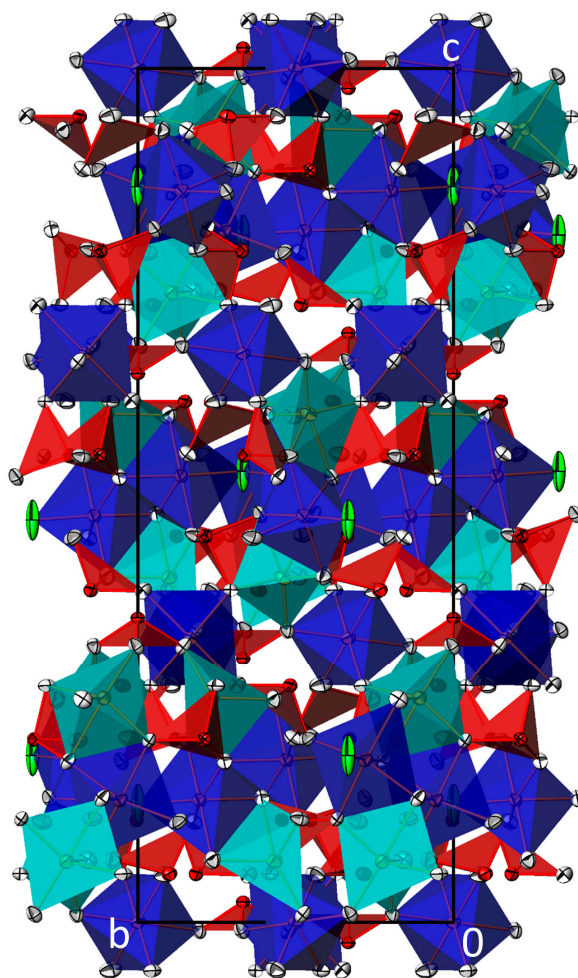


Figure 4. The crystal structures of $\text{Co}_{15}(\text{TeO}_3)_{14}(\text{OH})_2$ in a projection along $[100]$. $[\text{CoO}_6]$ and $[\text{CoO}_5\text{OH}]$ octahedra (Co1, Co3) are dark blue, $[\text{CoO}_5]$ polyhedra (Co2) are turquoise and $[\text{TeO}_3]$ polyhedra are red; the O8 atoms associated with the OH function are emphasized in green. Displacement ellipsoids are as in Figure 2.

The quantitative structural comparison between $\text{Co}_{15}(\text{TeO}_3)_{14}(\text{OH})_2$, as the reference structure, with isotopic $\text{Mn}_{15}(\text{TeO}_3)_{14}(\text{OH})_2$ and $\text{Co}_{15}(\text{TeO}_3)_{14}\text{F}_2$, is provided in Table 3. Atomic displacements for atom pairs in the structures, numerical values for the degree of lattice distortion (S), the arithmetic mean (d_{av}) of all distances and the measure of similarity (Δ) are compiled. On the whole, the absolute displacements for atom pairs are greater with respect to $\text{Mn}_{15}(\text{TeO}_3)_{14}(\text{OH})_2$ than to $\text{Co}_{15}(\text{TeO}_3)_{14}\text{F}_2$. Except for the OH group, which is substituted with an F atom, all atoms in $\text{Co}_{15}(\text{TeO}_3)_{14}\text{F}_2$ remain the same, whereas all transition metal atoms are replaced with respect to $\text{Mn}_{15}(\text{TeO}_3)_{14}(\text{OH})_2$. In the latter case, the larger ionic radii of Mn^{II} (0.75 Å for a coordination number of 5, 0.83 Å for a coordination number of 6 compared to Co^{II} with 0.67 and 0.745 Å, respectively [35]) are responsible for the higher atomic displacements, and consequently cause higher numbers for S and d_{av} , and therefore a structure with a lower similarity. However, in both cases, the highest displacement is observed for atom O8, which is associated with the OH group. The correspondent functionality as a donor for hydrogen bonding interactions, despite being weak in the present case, strongly influences its displacement in the isotopic structures. On the one hand, the replacement of OH through F leads to the disappearance of hydrogen bonding interactions. On the other hand, the larger Mn^{II} ions evoke an expansion of the entire structure, which also has an impact on the hydrogen bonding scheme with modified donor...acceptor distances.

Table 3. Comparison of $\text{Co}_{15}(\text{TeO}_3)_{14}(\text{OH})_2$ as the reference structure with isotypic $\text{Mn}_{15}(\text{TeO}_3)_{14}(\text{OH})_2$ and $\text{Co}_{15}(\text{TeO}_3)_{14}\text{F}_2$. Atom pairs are given with their absolute distances $|u|/\text{\AA}$, as well as the degree of lattice distortion (S), the arithmetic mean of the distances ($d_{\text{av}}/\text{\AA}$) and the measure of similarity (Δ).

Atom/Wyckoff Position		$\text{Mn}_{15}(\text{TeO}_3)_{14}(\text{OH})_2$	$\text{Co}_{15}(\text{TeO}_3)_{14}\text{F}_2$
M1	9 <i>e</i>	0	0
M2	18 <i>f</i>	0.0421	0.0188
M3	18 <i>f</i>	0.0396	0.0054
Te1	6 <i>c</i>	0.0093	0.0047
Te2	18 <i>f</i>	0.0556	0.0158
Te3	18 <i>f</i>	0.0706	0.0225
O1	18 <i>f</i>	0.0636	0.0073
O2	18 <i>f</i>	0.0263	0.0166
O3	18 <i>f</i>	0.0660	0.0229
O4	18 <i>f</i>	0.0307	0.0213
O5	18 <i>f</i>	0.0457	0.0146
O6	18 <i>f</i>	0.0282	0.0208
O7	18 <i>f</i>	0.0992	0.0320
O8/F1	6 <i>c</i>	0.3797	0.1441
S (a)		0.0165	0.0009
$d_{\text{av}}/\text{\AA}$ (b)		0.0573	0.0204
Δ (c)		0.016	0.005

(a) The degree of lattice distortion (S) is the spontaneous strain (sum of the squared eigenvalues of the strain tensor divided by 3). (b) The arithmetic mean (d_{av}) of all distances between atom pairs. (c) The measure of similarity (Δ) is a function of the differences in atomic positions (weighted by the multiplicities of the sites) and the ratios of the corresponding unit cell parameters of the structures.

3.3. Magnetic Properties

Figures 5a and 6a show the temperature dependence of the magnetization M collected under zero-field-cooled (ZFC) and field-cooled (FC) conditions in a small dc magnetic field ($H = 50$ Oe) for the two samples. The ZFC and FC curves of $\text{Co}_2(\text{TeO}_3)_2(\text{OH})_2$ reveal a sharp peak around 70 K (Figure 5a), suggesting an antiferromagnetic (AFM) ordering from a paramagnetic phase. In the case of $\text{Co}_{15}(\text{TeO}_3)_{14}(\text{OH})_2$, an antiferromagnetic-like peak is observed at $T \approx 18$ K, with an apparent excess moment [36] observed in low fields (see also the inset of Figure 6a). A weak irreversibility can be detected in the magnetization curves recorded in low fields below ≈ 70 K.

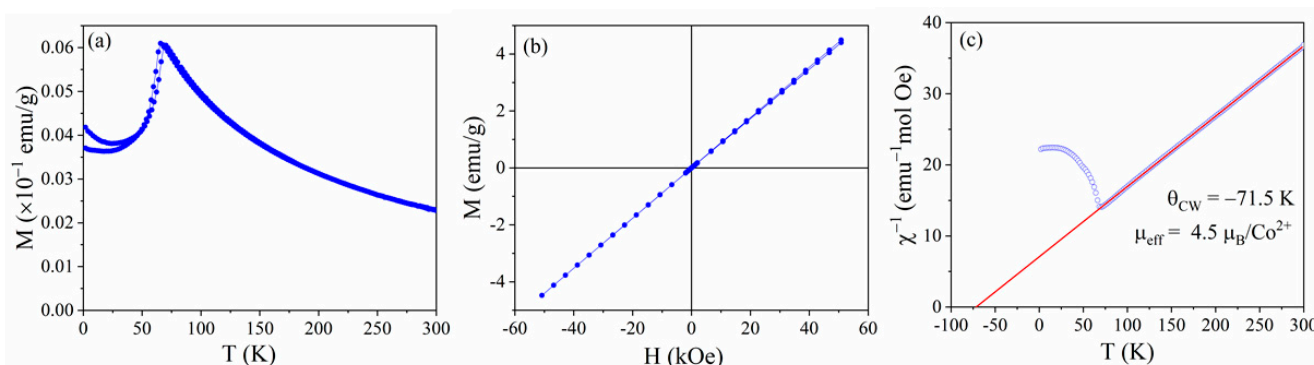


Figure 5. (a) Temperature dependence of the magnetization (M) in the field of 50 Oe of $\text{Co}_2(\text{TeO}_3)_2(\text{OH})_2$. (b) M versus H at 2 K. (c) Inverse susceptibility (χ^{-1}) versus T .

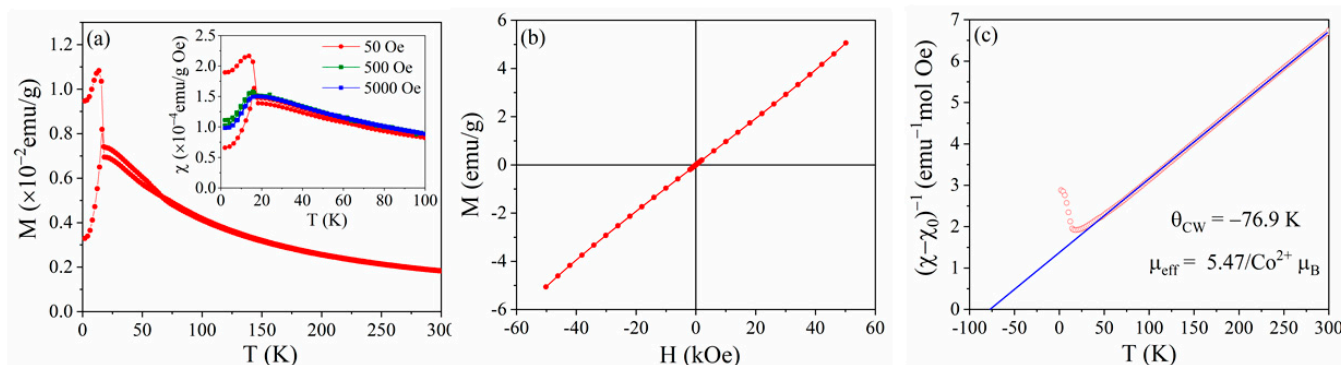


Figure 6. (a) M versus T of $\text{Co}_{15}(\text{TeO}_3)_{14}(\text{OH})_2$ at 50 Oe. Inset shows magnetic susceptibility $\chi = M/H$ vs. T recorded for different magnetic fields. (b) M versus H at 2 K. (c) $(\chi - \chi_0)^{-1}$ vs. T after correcting for a background contribution χ_0 (-0.0168 emu/mol·Oe).

The magnetic field dependence of the magnetization was recorded for both samples at $T = 2$ K, as shown in Figures 5b and 6b. Both $M(H)$ curves show the typical linear AFM behavior, with nearly zero coercive field. In the case of $\text{Co}_{15}(\text{TeO}_3)_{14}(\text{OH})_2$, a slight upturn of the magnetization seems to be observed above 40 kOe, possibly related to the reorientation discussed in the isotypic $\text{Co}_{15}(\text{TeO}_3)_{14}\text{F}_2$ [33].

The inverse of the magnetic susceptibility $\chi = M/H$ of the samples, recorded for $H = 5000$ Oe, was plotted vs. the temperature in Figures 5c and 6c in order to check the Curie–Weiss behavior of the susceptibility; $\chi = C/(T - \theta_{\text{CW}})$, where C and θ_{CW} represent the Curie constant and Curie–Weiss temperature, respectively. Good fits could be obtained, yielding the θ_{CW} and effective moment μ_{eff} ($C = N_{\text{A}} \mu_{\text{eff}}^2/3k_{\text{B}}$, where N_{A} and k_{B} are the Avogadro number and Boltzmann constant, respectively); values are listed in Table 4. For both samples, the obtained μ_{eff} value is higher than the spin-only value ($\mu_{\text{spin}} = 3.87 \mu_{\text{B}}$) of Co^{II} ($3d^7$, $S = 3/2$), which implies a significant orbital moment contribution. In general, μ_{eff} values exceeding the spin-only value are commonly observed for Co^{II} in an oxidic environment, including tellurium-containing corundum-related Co_3TeO_6 [7], A_2CoTeO_6 perovskites [37] or $\text{Co}_{15}(\text{TeO}_3)_{14}\text{F}_2$ [33]. The negative sign of θ_{CW} and its magnitude confirm the significant AFM interaction between the nearest Co^{II} spins present in both samples. While the Néel temperature T_{N} is found to appear near $-\theta_{\text{CW}}$ in the case of $\text{Co}_2(\text{TeO}_3)(\text{OH})_2$, T_{N} is significantly lower than $-\theta_{\text{CW}}$ for $\text{Co}_{15}(\text{TeO}_3)_{14}(\text{OH})_2$, which suggests some magnetic frustration [38] in the latter case. $\text{Co}_2(\text{TeO}_3)(\text{OH})_2$ undergoes an AFM transition below 70 K, akin to $\text{Co}_2(\text{SeO}_3)(\text{OH})_2$ [32], which shows a similar structural set-up, with chains and dimers condensed into a layered arrangement.

Table 4. Parameters obtained from the $M(T)$ curves and Curie–Weiss fitting of $\chi^{-1}(T)$. The ZFC/FC peak temperature is given as an estimation of T_{N} .

Compound	T_{N} (K)	θ_{CW} (K)	C (emu·K/mol·Oe)	$\mu_{\text{eff}}/\text{Co}^{2+}$ (μ_{B})
$\text{Co}_2(\text{TeO}_3)(\text{OH})_2$	70	−71.5	10.12	6.36
$\text{Co}_{15}(\text{TeO}_3)_{14}(\text{OH})_2$	18	−76.9	56.14	5.47

Expectedly, the overall magnetic behavior of $\text{Co}_{15}(\text{TeO}_3)_{14}(\text{OH})_2$ is qualitatively similar to that of isotypic $\text{Co}_{15}(\text{TeO}_3)_{14}\text{F}_2$ [33], where only the F and OH group is interchanged. In the case of $\text{Co}_{15}(\text{TeO}_3)_{14}(\text{OH})_2$, the frustration parameter $|\theta_{\text{CW}}/T_{\text{N}}|$ is slightly lower than that for the oxidofluoride (≈ 4.3 vs. 6.6). The observed magnetic frustration in $\text{Co}_{15}(\text{TeO}_3)_{14}(\text{OH})_2$, the excess moment detected in low magnetic fields, and the high-field non-linearity in $M(H)$ curves, suggest a complex spin structure associated with the specific coordination of the magnetic Co^{II} cations.

3.4. IR Spectroscopy

The IR spectra of the title compounds (Figures 7 and 8) can be divided into two vibrational parts, viz. the one characteristic for OH vibrations and the one from the $[\text{TeO}_3]$ groups and lattice vibrations of the different kinds of polyhedra around Co^{II} .

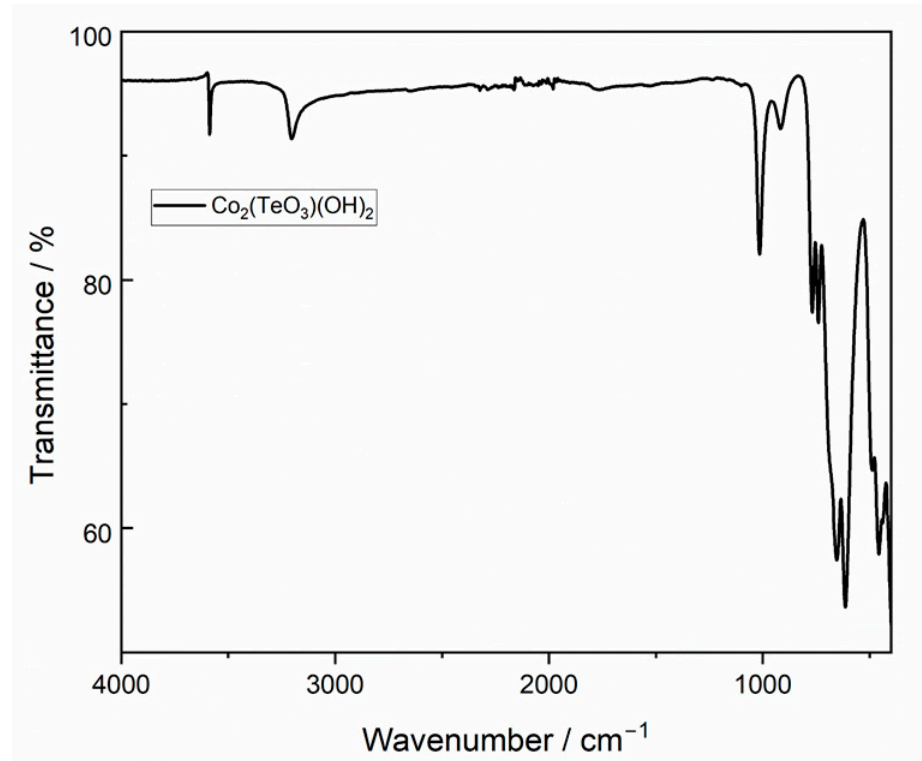


Figure 7. IR spectrum of $\text{Co}_2(\text{TeO}_3)(\text{OH})_2$.

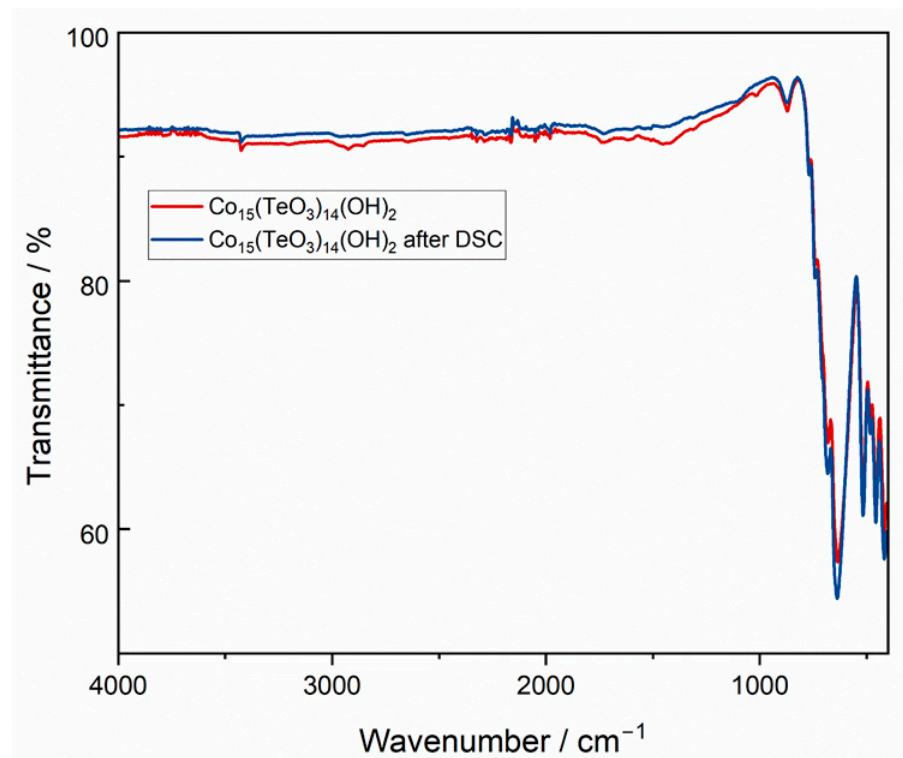


Figure 8. IR spectrum of $\text{Co}_{15}(\text{TeO}_3)_{14}(\text{OH})_2$ prior and after heat treatment at 580 °C.

$\text{Co}_2(\text{TeO}_3)(\text{OH})_2$ shows two OH stretching vibration bands at 3570 cm^{-1} and at 3202 cm^{-1} , respectively. The first band is associated with the OH group (O1) without an acceptor group for hydrogen bonding, which explains the rather sharp band profile and the high wavenumber. In comparison, the broad band and the red-shift of about 370 wave numbers for the second OH vibration (O2) indicates a clear participation in a hydrogen bonding interaction of a medium–strong nature. The application of Libowitzky’s empirical correlation between OH stretching and O–H \cdots O hydrogen bond lengths [39] results in an expected O \cdots O distance of 2.705 \AA , deviating only slightly from the experimental value of 2.730 \AA as determined from the X-ray diffraction study. The bending modes for the two OH vibrations are observed at 1016 and 917 cm^{-1} , in agreement with other solids containing OH groups, e.g., for various zinc hydroxy compounds, where these bands were observed between 1015 and 755 cm^{-1} [40], or for the phylломanganate birnessite that contains $\text{Mn}^{\text{II}}\text{–OH}$ and $\text{Mn}^{\text{III}}\text{–OH}$ groups, the bending vibrations of which were assigned in the range $1170\text{–}900\text{ cm}^{-1}$ [41].

In agreement with the crystal structure of $\text{Co}_{15}(\text{TeO}_3)_{14}(\text{OH})_2$, which comprises only one OH function (O8), the IR spectrum shows one OH stretching vibration band at 3425 cm^{-1} , albeit with a very weak intensity. The latter might be correlated with the low amount of OH in the compound (two OH groups related to an overall of 75 atoms in the formula). The position of this band suggests a significantly weaker hydrogen bonding interaction than that for the second OH group in $\text{Co}_2(\text{TeO}_3)(\text{OH})_2$. The correlation function reveals an expected value of 2.817 \AA . In fact, a possible O acceptor atom (O3) is located at 2.877 \AA from O2. However, the corresponding (H)O8 \cdots O3 donor \cdots acceptor group is not associated with an interpolyhedral distance (as usual) but is part of the $[\text{Co}_3\text{O}_5(\text{OH})]$ polyhedron, which makes a direct participation of O3 in hydrogen bonding unlikely. Without a clear localization of the corresponding H atom, the true nature of the hydrogen bonding situation thus remains unclear. The bending mode of the OH vibration at 871 cm^{-1} is in the same range as the ones given above.

The lower wavenumber part of the spectra is dominated by the Te–O vibrations, with a typical range between 800 and 600 cm^{-1} for the Te–O stretching vibrations [42], with the most prominent bands positioned at 768 , 740 , 654 and 613 cm^{-1} for $\text{Co}_2(\text{TeO}_3)(\text{OH})_2$ and 741 , 681 and 635 cm^{-1} for $\text{Co}_{15}(\text{TeO}_3)_{14}(\text{OH})_2$. Bands with lower wavenumbers between 600 and 500 cm^{-1} are assigned to Te–O bending vibrations [43,44], or may already occur from Co–O lattice vibrations.

3.5. Thermal Behavior

Under the conditions chosen for the TG/DSC study, $\text{Co}_2(\text{TeO}_3)(\text{OH})_2$ is stable up to $\approx 450\text{ }^\circ\text{C}$, as indicated by the very similar onsets of the endothermic DSC signal and of the mass loss in the TG curve (Figure 9). The DSC signal is split (maxima at 494 and $506\text{ }^\circ\text{C}$), indicating two separate incidents that, however, are not resolved in the TG curve. The continuous mass loss of 5.6% lasts to $525\text{ }^\circ\text{C}$ and corresponds to the loss of one water molecule per formula unit (theory 5.5%). The products after heat treatment, as revealed by PXRD, are $\text{Co}_6\text{Te}_5\text{O}_{16}$ and CoO in an approximate ratio of 3:1.

$\text{Co}_{15}(\text{TeO}_3)_{14}(\text{OH})_2$ shows remarkable thermal stability. TG and DSC measurements are featureless, indicating neither a structural change nor a decomposition in the chosen temperature range ($30\text{–}580\text{ }^\circ\text{C}$). In fact, the sample that had been subjected to the DSC measurement exhibited the same IR spectrum after heat treatment (Figure 8). Moreover, a single crystal from the DSC sample after heat treatment, selected for the X-ray diffraction study, showed an unchanged crystal structure. The same applies for polycrystalline material (see supplementary Figure S2).

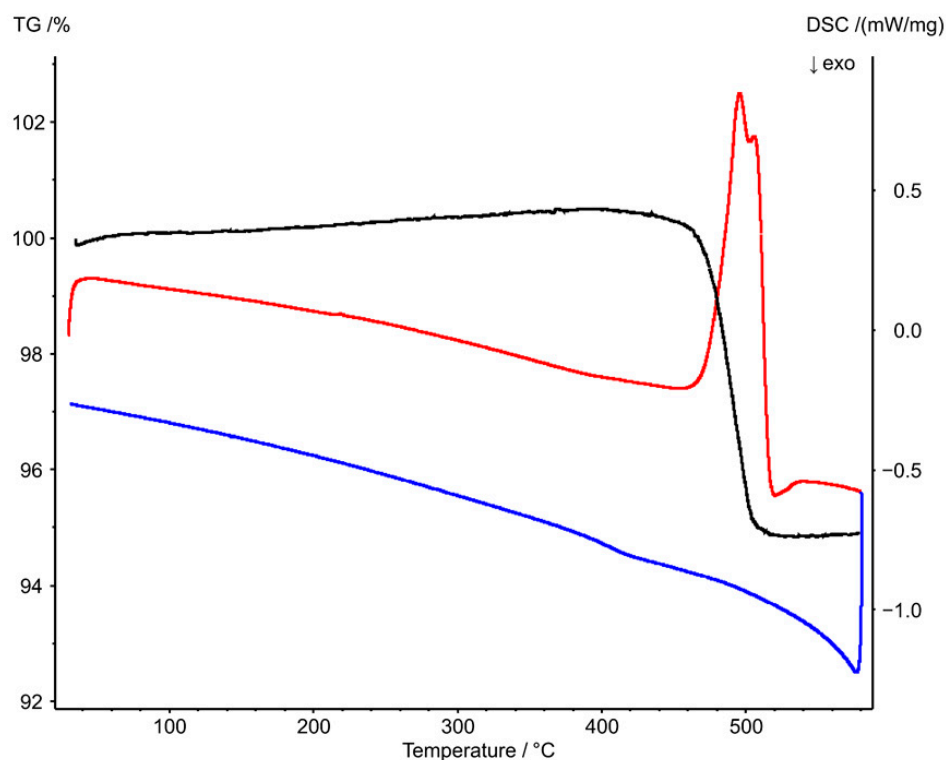


Figure 9. $\text{Co}_2(\text{TeO}_3)(\text{OH})_2$: TG curve (black) and DSC curves on heating (red) and cooling (blue).

4. Conclusions

The cobalt(II) oxidotellurates(IV) $\text{Co}_2(\text{TeO}_3)(\text{OH})_2$ and $\text{Co}_{15}(\text{TeO}_3)_{14}(\text{OH})_2$ were simultaneously obtained with other reaction products under hydrothermal formation conditions. Through the variation of the OH^- concentration to higher pH values and subsequent processing of the solid reaction product, single-phase material of $\text{Co}_2(\text{TeO}_3)(\text{OH})_2$ could eventually be obtained, whereas $\text{Co}_{15}(\text{TeO}_3)_{14}(\text{OH})_2$ was always present as part of product mixtures. The unique crystal structure of $\text{Co}_2(\text{TeO}_3)(\text{OH})_2$ is built up from ${}^2_{\infty}[\text{Co}_2(\text{OH})_{6/3}\text{O}_{3/3}\text{O}_{2/2}\text{O}_{1/1}]^{4-}$ layers held together by stereoactive Te^{IV} atoms. Two hydrogen bonds of the type $\text{O}-\text{H}\cdots\text{O}$ are observed. One is an interaction of medium strength and consolidates the layered set-up of the crystal structure, whereas the other is of a very weak nature, as revealed by possible $\text{O}\cdots\text{O}$ donor \cdots acceptor interactions and OH vibration bands. The crystal structure of $\text{Co}_2(\text{TeO}_3)(\text{OH})_2$ resembles that of the selenium(IV) analog $\text{Co}_2(\text{SeO}_3)(\text{OH})_2$, but exhibits a different crystal system (triclinic versus monoclinic). Magnetic measurements of $\text{Co}_2(\text{TeO}_3)(\text{OH})_2$ revealed an antiferromagnetic ordering temperature below 70 K. Above 450 °C, this phase decomposes into $\text{Co}_6\text{Te}_5\text{O}_{16}$ and CoO , in contrast to $\text{Co}_{15}(\text{TeO}_3)_{14}(\text{OH})_2$, which shows a remarkable thermal stability up to 580 °C without a structural change. The crystal structure of $\text{Co}_{15}(\text{TeO}_3)_{14}(\text{OH})_2$ is isotypic with previously reported $\text{Co}_{15}(\text{TeO}_3)_{14}\text{F}_2$. Since only the F and OH groups are interchanged, the magnetic properties of the two compounds are similar, with antiferromagnetic ordering temperatures below 10 K for $\text{Co}_{15}(\text{TeO}_3)_{14}\text{F}_2$ and below 18 K for $\text{Co}_{15}(\text{TeO}_3)_{14}(\text{OH})_2$, respectively.

Supplementary Materials: The following supporting information can be downloaded at: <https://www.mdpi.com/article/10.3390/cryst13020176/s1>, Figure S1: $\text{Co}_2(\text{TeO}_3)(\text{OH})_2$ —measured PXRD data; Figure S2: $\text{Co}_{15}(\text{TeO}_3)_{14}(\text{OH})_2$ —measured PXRD data.

Author Contributions: F.E.: Conceptualization; Investigation; Visualization; Data curation; Formal analysis; Writing—review and editing. M.W.: Conceptualization; Investigation; Visualization; Data curation; Resources; Supervision; Writing—original draft; Writing—review and editing. P.P.: Investigation; Data curation; Writing—original draft. R.M.: Investigation; Data curation; Writing—original draft. All authors have read and agreed to the published version of the manuscript.

Funding: We thank Stiftelsen Olle Engkvist Byggmästare (Grant No. 207-0427) for financial support.

Data Availability Statement: +15]Part of the data presented in this study are available in The Cambridge Crystallographic Data Centre (CCDC) and can be obtained free of charge via www.ccdc.cam.ac.uk/structures.

Acknowledgments: The X-ray centre of the TU Wien is acknowledged for providing free access to single crystal and powder X-ray diffraction instruments.

Conflicts of Interest: The authors declare no conflict of interest.

References

1. Kohn, K.; Akimoto, S.; Uesu, Y.; Asai, K. Crystal Structure and Magnetic Properties of MnTeO_3 , CoTeO_3 and NiTeO_3 . *J. Phys. Soc. Jpn.* **1974**, *37*, 1169. [CrossRef]
2. Iasir, A.R.M.; Lombardi, T.; Lu, Q.; Mofrad, A.M.; Vaninger, M.; Zhang, X.; Singh, D.J. Electronic and magnetic properties of perovskite selenite and tellurite compounds: CoSeO_3 , NiSeO_3 , CoTeO_3 , and NiTeO_3 . *Phys. Rev. B* **2020**, *101*, 045107. [CrossRef]
3. Patel, A.K.; Panda, M.R.; Rani, E.; Singh, H.; Samatham, S.S.; Nagendra, A.; Jha, S.N.; Bhattacharyya, D.; Suresh, K.G.; Mitra, S. Unique Structure-Induced Magnetic and Electrochemical Activity in Nanostructured Transition Metal Tellurates $\text{Co}_{1-x}\text{Ni}_x\text{TeO}_4$ ($x = 0, 0.5$, and 1). *ACS Appl. Energy Mater.* **2020**, *3*, 9436–9448. [CrossRef]
4. Ivanov, S.A.; Tellgren, R.; Ritter, C.; Nordblad, P.; Mathieu, R.; Andre, G.; Golubko, N.V.; Politova, E.D.; Weil, M. Temperature-dependent multi-k magnetic structure in multiferroic Co_3TeO_6 . *Mater. Res. Bull.* **2012**, *47*, 63–72. [CrossRef]
5. Lee, C.-H.; Wang, C.-W.; Zhao, Y.; Li, W.-H.; Lynn, J.W.; Harris, A.B.; Rule, K.; Yang, H.-D.; Berger, H. Complex magnetic incommensurability and electronic charge transfer through the ferroelectric transition in multiferroic Co_3TeO_6 . *Sci. Rep.* **2017**, *7*, 6437. [CrossRef] [PubMed]
6. Reichartzeder, D.; Wildner, M.; Weil, M.; Ivanov, S.A.; Stash, A.; Chen, Y.-S. Crystal chemistry, optical spectroscopy and crystal field calculations of Co_3TeO_6 and solid solutions $\text{Co}_{3-x}\text{Zn}_x\text{TeO}_6$. *Eur. J. Inorg. Chem.* **2018**, *2018*, 4221–4233. [CrossRef]
7. Hudl, M.; Mathieu, R.; Ivanov, S.A.; Weil, M.; Carolus, V.; Lottermoser, T.; Fiebig, M.; Tokunaga, Y.; Taguchi, Y.; Tokura, Y.; et al. Complex magnetism and magnetic-field-driven electrical polarization of Co_3TeO_6 . *Phys. Rev. B* **2011**, *84*, 180404. [CrossRef]
8. Selb, E.; Buttlar, T.; Janka, O.; Tribus, M.; Ebbinghaus, S.G.; Heymann, G. Multianvil high-pressure/high-temperature synthesis and characterization of magnetoelectric HP- Co_3TeO_6 . *J. Mater. Chem. C* **2021**, *9*, 5486–5496. [CrossRef]
9. Podchertsev, S.; Barrier, N.; Pautrat, A.; Suard, E.; Retuerto, M.; Alonso, J.A.; Fernández-Díaz, M.T.; Rodríguez-Carvajal, J. Influence of Polymorphism on the Magnetic Properties of Co_5TeO_8 Spinel. *Inorg. Chem.* **2021**, *60*, 13990–14001. [CrossRef]
10. Becker, R.; Johnsson, M.; Berger, H. A new synthetic cobalt tellurate: Co_3TeO_6 . *Acta Crystallogr. Sect. C* **2006**, *62*, i67–i69. [CrossRef]
11. Trömel, M.; Scheller, T. Die Kristallstruktur von $\text{Co}_6\text{Te}_5\text{O}_{16}$. *Z. Anorg. Allg. Chem.* **1976**, *427*, 229–234. [CrossRef]
12. Irvine, J.T.S.; Johnston, M.G.; Harrison, W.T.A. Lone-pair containment in closed cavities. The $\text{MTe}_6\text{O}_{13}$ ($M = \text{Mn}, \text{Ni}, \text{Co}$) family of ternary oxides. *Dalton Trans.* **2003**, 2641–2645. [CrossRef]
13. Feger, C.R.; Schimek, G.L.; Kolis, J.W. Hydrothermal synthesis and characterization of $\text{M}_2\text{Te}_3\text{O}_8$ ($M = \text{Mn}, \text{Co}, \text{Ni}, \text{Cu}, \text{Zn}$): A series of compounds with the spiroffite structure. *J. Solid State Chem.* **1999**, *143*, 246–253. [CrossRef]
14. Perez, G.; Lasserre, F.; Moret, J.; Maurin, M. Structure cristalline des hydroxytellurites de nickel et de cobalt. *J. Solid State Chem.* **1976**, *17*, 143–149. [CrossRef]
15. Poupon, M.; Barrier, N.; Pautrat, A.; Petit, S.; Perez, O.; Bazin, P. Investigation of $\text{Co}_6(\text{OH})_3(\text{TeO}_3)_4(\text{OH})\sim 0.9(\text{H}_2\text{O})$: Synthesis, crystal and magnetic structures, magnetic and dielectric properties. *J. Solid State Chem.* **2019**, *270*, 147–155. [CrossRef]
16. Eder, F.; Weil, M.; Missen, O.P.; Kolitsch, U.; Libowitzky, E. The Family of $\text{M}^{\text{II}}_3(\text{Te}^{\text{IV}}\text{O}_3)_2(\text{OH})_2$ ($M = \text{Mg}, \text{Mn}, \text{Co}, \text{Ni}$) Compounds—Prone to Inclusion of Foreign Components into Large Hexagonal Channels. *Crystals* **2022**, *12*, 1380. [CrossRef]
17. Eder, F.; Marsollier, A.; Weil, M. Structural Studies on Synthetic $\text{A}_{2-x}[\text{M}_2(\text{TeO}_3)_3]\cdot n\text{H}_2\text{O}$ Phases ($A = \text{Na}, \text{K}, \text{Rb}, \text{Cs}$; $M = \text{Mn}, \text{Co}, \text{Ni}, \text{Cu}, \text{Zn}$) with Zemannite-Type Structures. *Min. Petrolog.* **2023**, accepted.
18. Degen, T.; Sadki, M.; Bron, E.; König, U.; Nénert, G. The HighScore suite. *Powder Diffr.* **2014**, *29*, 13–18. [CrossRef]
19. APEX-4 and SAINT; Bruker AXS Inc.: Madison, WI, USA, 2021.
20. Krause, L.; Herbst-Irmer, R.; Sheldrick, G.M.; Stalke, D. Comparison of silver and molybdenum microfocus X-ray sources for single-crystal structure determination. *J. Appl. Cryst.* **2015**, *48*, 3–10. [CrossRef]
21. Sheldrick, G.M. SHELXT-Integrated space-group and crystal-structure determination. *Acta Crystallogr. Sect. A* **2015**, *71*, 3–8. [CrossRef]
22. Sheldrick, G.M. Crystal structure refinement with SHELXL. *Acta Crystallogr. Sect. C* **2015**, *71*, 3–8. [CrossRef] [PubMed]
23. ATOMS for Windows; Shape Software: Kingsport, TN, USA, 2006.

24. Eder, F.; Weil, M. Phase formation studies and crystal structure refinements in the Mn^{II}/Te^{IV}/O/(H) system. *Z. Anorg. Allg. Chem.* **2022**, *648*, e202200205. [[CrossRef](#)]
25. Brown, I.D. *The Chemical Bond in Inorganic Chemistry: The Bond Valence Model*; Oxford University Press: Oxford, UK, 2002.
26. Brese, N.E.; O'Keeffe, M. Bond-valence parameters for solids. *Acta Crystallogr. Sect. B* **1991**, *47*, 192–197. [[CrossRef](#)]
27. Mills, S.J.; Christy, A.G. Revised values of the bond-valence parameters for Te^{IV}—O, Te^{VI}—O and Te^{IV}—Cl. *Acta Crystallogr. Sect. B* **2013**, *69*, 145–149. [[CrossRef](#)] [[PubMed](#)]
28. de la Flor, G.; Orbeno, D.; Tasci, E.; Perez-Mato, J.M.; Aroyo, M.I. Comparison of structures applying the tools available at the Bilbao Crystallographic Server. *J. Appl. Crystallogr.* **2016**, *49*, 653–664. [[CrossRef](#)]
29. Aroyo, M.I.; Perez-Mato, J.M.; Capillas, C.; Kroumova, E.; Ivantchev, S.; Madariaga, G.; Kirov, G.; Wondratschek, H. Bilbao Crystallographic Server I: Databases and crystallographic computing programs. *Z. Kristallogr.* **2006**, *221*, 15–27. [[CrossRef](#)]
30. Gagné, O.C.; Hawthorne, F.C. Bond-length distributions for ions bonded to oxygen: Results for the transition metals and quantification of the factors underlying bond-length variation in inorganic solids. *IUCr* **2020**, *7*, 581–629. [[CrossRef](#)]
31. Christy, A.; Mills, S.J.; Kampf, A. A review of the structural architecture of tellurium oxycompounds. *Mineral. Mag.* **2016**, *80*, 415–545. [[CrossRef](#)]
32. Ruidan Zhong, R.; Guo, S.; Ni, D.; Cava, R.J. Dicobalt (II) hydroxo-selenite: Hydrothermal synthesis, crystal structure and magnetic properties of Co₂SeO₃(OH)₂. *J. Solid State Chem.* **2020**, *285*, 121250. [[CrossRef](#)]
33. Lü, M.; Jiang, J.; Zhu, B.; Zhao, Y.; Zhu, T.; Yang, H.; Jin, Y.; Kabbour, H.; Choi, K.Y.; Harrison, W.T.A. Lone-pair self-containment in pyritohedron-shaped closed cavities: Optimized hydrothermal synthesis, structure, magnetism and lattice thermal conductivity of Co₁₅F₂(TeO₃)₁₄. *Dalton Trans.* **2020**, *49*, 2234–2243. [[CrossRef](#)]
34. Addison, A.W.; Rao, N.T.; Reedijk, J.; van Rijn, J.; Verschoor, G.C. Synthesis, structure, and spectroscopic properties of copper(II) compounds containing nitrogen–sulphur donor ligands; the crystal and molecular structure of aqua [1,7-bis(N-methylbenzimidazol-2'-yl)-2,6-dithiaheptane]copper(II) perchlorate. *J. Chem. Soc., Dalton Trans.* **1984**, 1349–1356. [[CrossRef](#)]
35. Shannon, R.D. Revised Effective Ionic Radii and Systematic Studies of Interatomic Distances in Halides and Chalcogenides. *Acta Crystallogr. Sect. A* **1976**, *32*, 751–767. [[CrossRef](#)]
36. Joshi, D.C.; Nordblad, P.; Mathieu, R. Ferromagnetic excess moments and apparent exchange bias in FeF₂ single crystals. *Sci. Rep.* **2019**, *9*, 18884. [[CrossRef](#)]
37. Mathieu, R.; Ivanov, S.A.; Tellgren, R.; Nordblad, P. Influence of the A cation on the low-temperature antiferromagnetism of ordered antiferroelectric A₂CoTeO₆ perovskites. *Phys. Rev. B* **2011**, *83*, 174420. [[CrossRef](#)]
38. Ramirez, A.P. Strongly Geometrically Frustrated Magnets. *Annu. Rev. Mater. Sci.* **1994**, *24*, 453–480. [[CrossRef](#)]
39. Libowitzky, E. Correlation of O-H stretching frequencies and O-H . . . O hydrogen bond lengths in minerals. *Monatsh. Chem.* **1999**, *130*, 1047–1059. [[CrossRef](#)]
40. Srivastava, D.E.A.; Secco, A. Studies on metal hydroxy compounds. II. Infrared spectra of zinc derivatives ε-Zn(OH)₂, β-ZnOHCl, ZnOHF, Zn₅(OH)₈Cl₂, and Zn₆(OH)₈Cl₂·H₂O. *Can. J. Chem.* **1967**, *45*, 585–588. [[CrossRef](#)]
41. Zhao, W.; Liu, F.; Feng, X.; Tan, W.; Qiu, G.; Chen, X. Fourier transform infrared spectroscopy study of acid birnessites before and after Pb. *Clay Miner.* **2012**, *47*, 191–204. [[CrossRef](#)]
42. Szaller, Z.; Kovács, L.; Pöpl, L. Comparative Study of Bismuth Tellurites by Infrared Absorption Spectroscopy. *J. Solid State Chem.* **2000**, *152*, 392–396. [[CrossRef](#)]
43. Farmer, V.C. (Ed.) *Mineralogical Society Monograph 4: The Infrared Spectra of Minerals*; The Mineralogical Society: London, UK, 1974.
44. Rumsey, M.S.; Welch, M.D.; Mo, F.; Kleppe, A.K.; Spratt, J.; Kampf, A.R.; Raanes, M.P. Millsite CuTeO₃·2H₂O: A new polymorph of teinite from Gråurdjället, Oppdal kommune, Norway. *Mineral. Mag.* **2018**, *82*, 433–444. [[CrossRef](#)]

Disclaimer/Publisher's Note: The statements, opinions and data contained in all publications are solely those of the individual author(s) and contributor(s) and not of MDPI and/or the editor(s). MDPI and/or the editor(s) disclaim responsibility for any injury to people or property resulting from any ideas, methods, instructions or products referred to in the content.